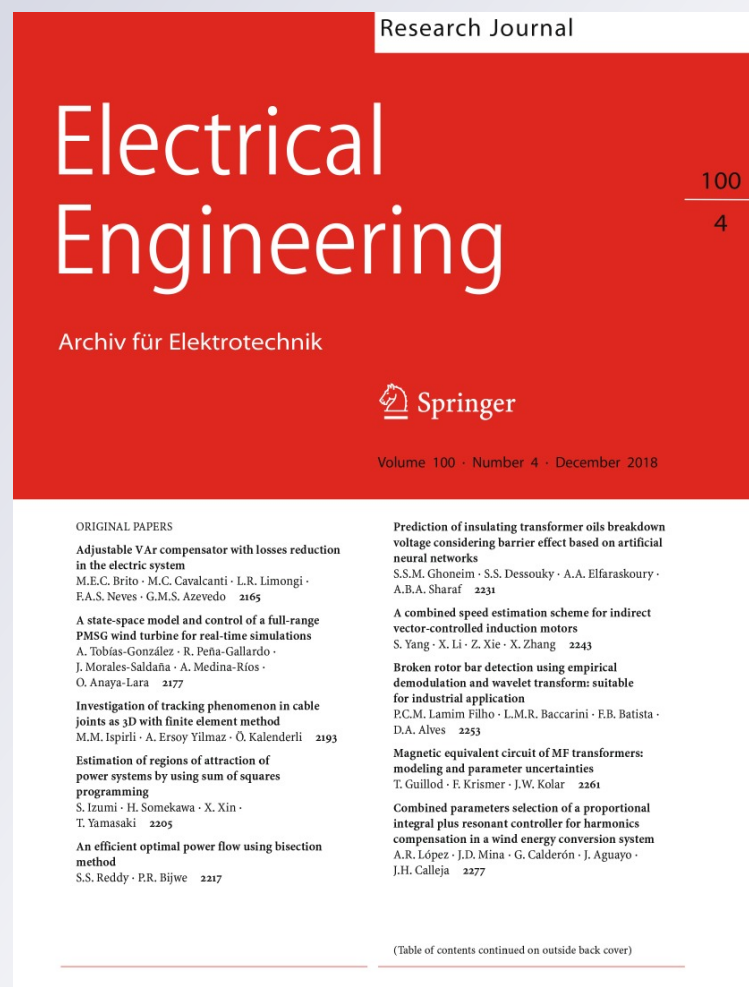# Optimisation and design comparison of 10-kW and 3-MW PM flux-switching machines for geared medium-speed wind power generators

Udochukwu B. Akuru & Maarten J. Kamper

Springer

Springer

ORIGINAL PAPER

CrossMark

Optimisation and design comparison of 10-kW and 3-MW PM flux-switching machines for geared medium-speed wind power generators

Udochukwu B. Akuru[1,2] · Maarten J. Kamper[1]

Abstract

The paper details the design optimisation and comparison of two different rare-earth permanent magnet flux-switching machines (PM-FSMs)—12/10 and 12/14—for geared medium-speed wind power generators. The focus is mainly on trade-offs in the performance of these two machines at 10 kW and 3 MW power levels, with highlights on the multi-objective evolutionary optimal performance of small-scale to utility-scale wind turbines. Based on finite element analyses (FEA) and multi-objective design optimisation (MDO), different streams of optimal solutions are obtained and studied. As an indication of the potentials of the proposed PM-FSM wind generators, even for rare-earth-free concepts, the 3 MW designs portray significantly improved torque density thanks to the fixed rotor speed considered at both power levels, and also, smaller torque ripple profiles are conceived due to differences in the calculated saliency ratios, compared to their 10 kW designs. Another finding is based on the nonlinearity of the MDO process on the objective performance of the different machine topologies at the different power levels, which was necessitated by the optimal behaviour of certain design variables such as the split ratio, slot opening width, current density and PM width. Uncharacteristically, the results also reveal possibilities for higher efficiency in 12/14 machines compared to the 12/10 machines, due to positive relationships approximated from general evaluations conceived in the MDO search space in the former, for the split ratio and current density when plotted against the active mass. Lastly, a comparison between 2-D static and 3-D transient FEA processes on some selected benchmarks displayed good agreement.

Keywords Finite element analyses · Multi-objective design optimisation · Medium-speed drives · Flux-switching machines · Wind power generator

List of symbols

f_e	Frequency (Hz)
n_s	Mechanical speed (r/min)
N_r	Number of rotor poles
λ_M	PM flux linkage (Wb t)
I_d, I_q	dq axes currents (A)
L_d, L_q	dq axes inductances (H)
N_t	Number of turns per phase
κ_e	Leakage factor

✉ Udochukwu B. Akuru
  udochukwu.akuru@unn.edu.ng

1 Department of Electrical and Electronic Engineering, Stellenbosch University, Stellenbosch 7600, South Africa

2 Department of Electrical Engineering, University of Nigeria, Nsukka 410001, Nigeria

$\dot{B}_g$	Peak airgap flux density (T)
l_{st}	Stack length (mm)
τ_s	Stator pole pitch (mm)
c_s	Stator tooth arc factor
D_{out}	Stator outer diameter (mm)
M_A	Total active mass (kg)
M_{Cu}	Copper mass of phase windings (kg)
M_{FeR}	Rotor iron mass (kg)
M_{FeS}	Stator iron mass (kg)
M_k	Mass of a corresponding k iron core part (kg)
M_{PM}	PM mass (kg)
n	Number of similar iron core parts considered
V_d, V_q	dq axes voltages (V)
R_s	Phase resistance with end-winding effects (Ω)
C_m, σ and β	Steinmetz coefficients for core loss estimation
N_s	Number of slots
A_s	Electrical loading (A/mm)

η	Efficiency (%)
τ_e	Electromagnetic torque (Nm)
Λ_0	Split ratio
κ_L	Aspect ratio
P_{out}	Generator output power (kW or MW)
ω_e	Shaft speed (rad/s)
D_{in}	Stator inner diameter (mm)
n_s	Rated speed (r/min)
J	RMS current density (A/mm^2)
θ_{sF}	Slot fill factor
B_r	PM remanence (T)
μ_r	Relative permeability
pf	Power factor
g	Airgap length (mm)
b_{ps}	Stator tooth width (mm)
b_{pm}	Stator PM width (mm)
b_{sls}	Stator slot opening (mm)
h_{ys}	Stator yoke thickness (mm)
b_{pr}	Rotor tooth width (mm)
h_{yr}	Rotor yoke thickness (mm)
M_A	Active mass (kg)
κ_δ	Torque ripple (%)
$\tau_{e\,(min)}$	Instantaneous minimum value of τ_e (Nm)
$\tau_{e\,(max)}$	Instantaneous maximum value of τ_e (Nm)
N	Number of design parameters
F	Vector of objective functions
$\bar{x}$	Vector of design parameters
L, U	Lower and upper boundary limit parameters
G_1, G_2	Vector of inequality constraints

1 Introduction

Based on an increasing demand for large megawatts wind turbine systems, the need to reduce the cost of generation is becoming critical such that attention is now being directed towards the available wind generator drivetrains. The known wind generator drivetrains are low-speed (LS), medium-speed (MS) and high-speed (HS) drives. A summary of the drivetrain characteristics as shown in Table 1 indicates that MS drivetrains are preferable compromise to LS and HS systems. Because most MS drivetrains have 1- or 2-stage gearboxes coupled to moderate-sized wind generators, they lead to greater annual energy yield per generator cost at average wind speeds [1]. Some specific benefits of MS drivetrains include:

- Low structural, capital and operational costs: utilisation of simple 1- or 2-stage gearbox leading to smaller generator and drivetrain mass and lower costs of energy;
- Improved reliability and improved efficiency due to the absence of HS gearboxes known to cause failures; and

Table 1 Comparison of different drivetrain concepts

Parameter	HS	MS	LS
Speed margin	600–2000 r/min	40–600 r/min	4–35 r/min[a]
Mass	Lightest	Intermediate	Heaviest
Size	Smallest	Intermediate	Largest
Gearbox presence	Yes (3G[b])	Yes (1G/2G)	Absent
Generator type	IG/SG[c]	IG/SG	SG
Mechanical losses	High	Intermediate	Lowest
Electrical losses	Lowest	Intermediate	Highest
Cost	Gearbox[d]	Intermediate	Generator[d]

[a]Also depends on operating power level
[b]G gearbox stage
[c]IG induction generator, SG synchronous generator
[d]Highest cost

- Compact size of wind generators which lead to lower top head mass for easier logistics, as well as reduction in the tower materials required with a lighter nacelle is utilised.

On the other hand, PM flux-switching machines (PM-FSMs), which are not entirely new, belong to a class of stator-active machines with double saliency [2]. The operation of FSMs is such that it produces bipolar flux in the armature (stator) teeth as a result of modulation of the flux linkage with respect to change in rotor position (flux switching). In the absence of PMs, the field sources can equally be facilitated using wound fields (WFs) based on an appropriate orientation [3]. To this end, PM-FSMs are endowed with such qualities as high-power (torque) density, good thermal dissipation and a robust rotor structure. In addition, concentrated windings, similar to those in switched reluctance machines, are employed, leading to reduced end-winding length and losses. However, it must be said that the torque pulsations in FSMs are known to be very severe [4].

Just like in typical PM synchronous machine topologies, PM-FSMs are also designed as axial flux (with disc-type rotors), transverse flux (with pancake or disc-type rotors) or radial flux (with cylindrical rotors). Meanwhile, other novel radial-flux topologies such as the segmented-rotor WF-FSM [5], overlap winding PM-FSM [6] and magnetically geared partitioned-stator PM-FSM [7] have also been presented and are discussed in recent times.

Oftentimes, radial-flux PM-FSMs have been applied in in-wheel traction for EV/HEV motor operation at low power levels [8–10]. In terms of wind generator applications, transverse-flux and axial-flux PM-FSMs have been popular in LS drivetrains at low power levels [11–14], except in [15], whereby a high-temperature superconductor (HTS) radial-flux WF-FSM with high-power density is proposed

Fig. 1 Proposed PM-FSM geared medium-speed wind energy system
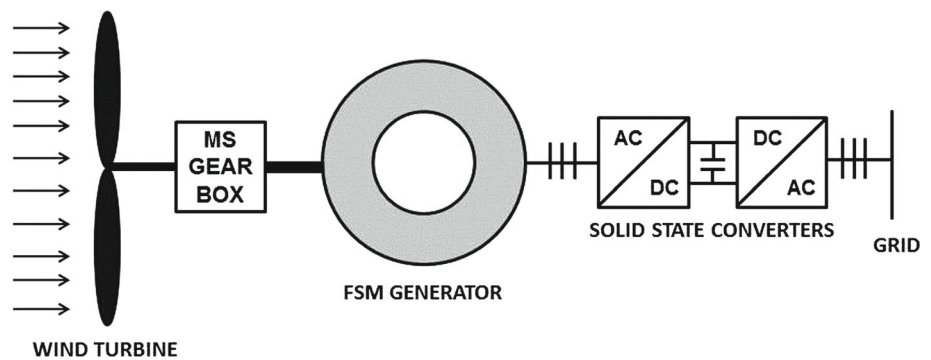
and compared to replace its PM-FSM counterpart. But unlike the radial-flux designs, transverse-flux and axial-flux PM-FSMs manifest in very complex structures which are bound to increase their manufacturing and assembly costs. Besides, as already shown in Table 1, LS generators are not attractive because they are heavier and more expensive.

With regard to HS systems, not much is documented for PM-FSMs. In [16], a new single-phase magnetless FSM was developed for rooftop wind power generation with rated power of less than 1 kW. Also, a study in [17] demonstrated the feasibility of PM-FSMs for so-called high-speed and high-power (50 kW) generator application. Apart from issues regarding high gearbox reliability, PM-FSMs designed for HS are prone to very high core losses [18]. As for MS drivetrains, the application of radial-flux PM-FSM to MS wind generator drivetrains was first contrived in [19], where the 12-stator slots/10-rotor pole (12/10) machine was optimised by deterministic techniques and compared (at par) to a 12/14 machine, at 4 kW output power. Similarly, in [20], both the 12/10 and 12/14 PM-FSMs were designed, based on parameter variation, and compared at 400 r/min, 1.5 kW power, without reference to any application requirements. In both studies, the higher torque and lower torque ripple performance of the 12/14 over the 12/10 were elucidated. However, the limitation of using gradient-based technique in the design optimisation and comparison of both PM-FSM topologies were clearly revealed in [19], showing that the optimisation process can lead to hard problems within the nonlinear multi-modal search space.

Therefore, it goes without saying that for a more robust optimisation, the use of metaheuristic optimisation algorithms in the design of PM-FSMs cannot be overemphasised. Moreover, because existing studies concentrated on the analyses of small kW power ratings, which may not be representative of the power levels in large wind turbines, there is need to investigate the performance of FSMs as it is scaled from 10 kW to 3 MW power levels. Thus, the current study is on the multi-objective design optimisation (MDO) and design comparison of the 12/10 and 12/14 rare-earth PM-FSMs for the proposed wind generators at 10 kW and 3 MW

power levels. Due to potentially different performance characteristics for the prescribed power range, as well as the proliferation of utility-scale wind turbines, this kind of study is deemed necessary. Hence, the focus of this paper is on trade-offs which may result from such comparative study on PM-FSM wind generators.

The proposed geared MS wind energy system is illustrated in Fig. 1. Because torque density is critical to the generator mass, which in turn defines the nacelle weight, a reduced generator mass is anticipated in the study. Also to be considered is the torque ripple, which, if unusually high, can be hazardous to the MS gearbox, leading to mechanical vibrations. Of course, other important penalties such as high-power factor and efficiency which are required to improve the overall drivetrain efficiency are also carefully considered in the study.

2 Design approach and model creation

2.1 Sizing procedure

The layouts for the three-phase 12/10 and 12/14 PM-FSM result in balanced magnetic fields. However, the 12/14 topology, with a higher fundamental frequency, has its phase "B" and "C" coils swapped compared to the 12/10 design. For the same operating conditions, the 12/14 may result in higher fundamental frequency, torque and induced phase voltages than the 12/10 machine based on the following expressions:

$$f_e = \frac{n_s N_r}{60}, \tag{1}$$

$$\tau_e = \frac{3}{2} N_r \big(I_q \lambda_M + I_d I_q (L_d - L_q) \big), \tag{2}$$

$$E_g = 2\pi f_e N_t \kappa_e \dot{B}_g l_{st} \tau_s c_s, \tag{3}$$

where n_s is the mechanical speed in r/min, N_r is the number of rotor poles, λ_M is the no-load flux linkage, I_d and I_q are the dq axes phase currents, L_d and L_q are the dq axes inductances, N_t is the number of turns per phase, κ_e is a factor to account

Table 2 Design specifications

Symbol	Specifications	10 kW	3 MW
n_s	Rated speed	360 r/min	
J	Current density	1–5 A/mm^2	
θ_{sF}	Slot fill factor	0.4	
B_r	PM remanence	1.2 T	
pf	Power factor	≥ 0.8	
η	Efficiency	$\geq 90\%$	$\geq 97\%$
g	Airgap length	0.7 mm	2.5–3 mm

Table 3 Material specifications

Material	Properties
Windings	Copper: $\rho_{Cu} = 2.07312 \times 10^{-8}$ Ωm
Laminations	NO fully processed electrical steel: M400-50A
Magnet	NdFeB PM ($\mu_r = 1.06$, $B_r = 0.4$ T)

for some leakage, $\dot{B}_g$ is the peak airgap flux density, l_{st} is the stack length of the lamination cores, τ_s is stator pole pitch, and c_s is the stator tooth arc factor.

To generate the initial geometries of the proposed PM-FSM topologies, the design specifications imposed for the 10 kW and 3 MW designs are given in Table 2, while the material specifications are provided in Table 3. With this information, the PM-FSMs are modelled according to the sizing equation as amended from [21] as follows:

$$D_{out} = \sqrt[3]{\frac{4\tau_e N_s}{\sqrt{2}\pi^2 N_r \kappa_e \kappa_L \Lambda_0^3 A_s \dot{B}_g \eta c_s}}, \qquad (4)$$

where D_{out} is the stator outer diameter, N_s is the number of slots for the phase windings, A_s is the electrical loading of the phase windings, and η is the efficiency of the machine, while κ_e, $\dot{B}_g$ and c_s are as earlier defined. The electromagnetic torque τ_e, split ratio Λ_0 and aspect ratio κ_L are expressed as

$$\tau_e = \frac{P_{out}}{\omega_e}; \quad \Lambda_0 = \frac{D_{in}}{D_{out}}; \quad \kappa_L = \frac{l_{st}}{D_{in}}, \qquad (5)$$

where P_{out} is the proposed generator outer power, ω_e is the proposed generator shaft speed in rad/s, D_{in} is the stator inner diameter, and l_{st} is as previously defined.

Based on the data supplied in Table 2, an initial stator outer diameter of the 12/10 machines is approximated using (4). For fair comparison, the same stator outer diameter is retained a priori for the 12/14 machines.

2.2 Topology modelling

The generic radial-flux PM-FSM structure is created by equating the stator tooth width (b_{ps}), the stator PM width (b_{pm}), the stator slot opening (b_{sls}), the stator yoke thickness (h_{ys}), the rotor tooth width (b_{pr}) and the rotor yoke thickness (h_{yr}) to the size of the stator pole pitch. The stator pole pitch defined as $\tau_s = \pi D_{in}/N_s$ determines the default values for each parameters expressed as

$$b_{ps} = b_{pm} = b_{sls} = h_{ys} = b_{pr} = h_{yr} = \frac{\tau_s}{4}. \qquad (6)$$

Based on these approximations, the resulting 2-D geometry is modelled as illustrated in Fig. 2. By utilising an in-house 2-D static FEA package, so-called SEMFEM [22], the electromagnetic performance of the created model can be analysed, with the end-winding effects analytically incorporated.

3 FEA multi-objective design optimisation

No doubt, the design optimisation of PM-FSMs presents a nonlinear multi-objective problem as portrayed in [19]. Thus, the best optimisation procedure is propagated when the problem is constrained and a multi-objective design is pursued. In the present scenario, where wind generator design is implied, certain key performance indices, such as minimum mass and torque ripple, are simultaneously optimised in order to increase the wind turbine cost savings and improve the drivetrain reliability, as well as declare any potential trade-offs. However, to proceed further, the following expressions are important to be defined:

$$M_A = M_{FeS} + M_{FeR} + M_{PM} + M_{Cu}, \qquad (7)$$

$$\delta = \frac{\tau_{e(max)} - \tau_{e(min)}}{\tau_e}, \qquad (8)$$

$$p_{out} = \frac{3}{2}(V_d I_d + V_q I_q), \qquad (9)$$

$$P_{Cu} = \frac{3}{2}(I_d^2 + I_q^2)R_s, \qquad (10)$$

$$P_{Core} = C_m f_e^\beta \sum_{k=1}^{n} \dot{B}_k^\sigma M_k, \qquad (11)$$

$$\eta = \frac{p_{out}}{p_{out} + P_{Cu} + P_{Core}}, \qquad (12)$$

$$pf = \cos\left(\tan^{-1}\left(\frac{V_d}{V_q}\right)\right). \qquad (13)$$

where M_A is the active mass, τ_e is the electromagnetic torque, κ_δ is the torque ripple, P_{out} is the output power, P_{Cu} is the copper loss, P_{Core} is the core loss defined by the iron and hysteresis losses, η is the efficiency, and pf symbolises the power
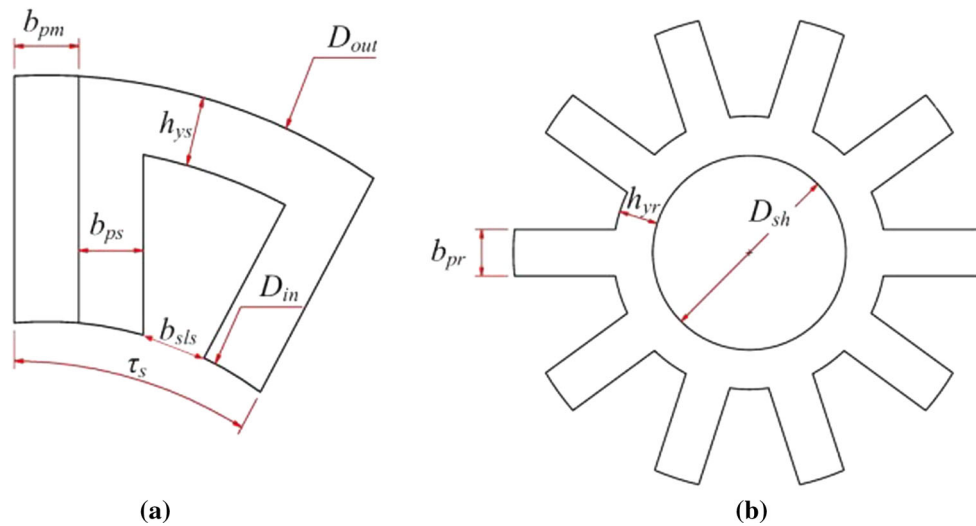
Fig. 2 Generic PM-FSM geometry: **a** stator segment and **b** rotor piece

factor. The other parameters are defined in the nomenclature list proceeding Sect. 1.

The MDO approach adopted is to concurrently minimise M_A and κ_δ while constraining P_{out}, η and pf to the specifications declared in Table 2. The objective functions are proposed in two combinatorial problems, weighted equally. Thus, as indicated, two different constraints are evinced because of the two different power levels under investigation.

The MDO problem is defined (14), subject to boundary constraints on N design parameters (15) and design constraints based on the different power levels (16) and (17), as follows:

$$\text{minimise } F(\bar{x}) = \begin{bmatrix} M_A & \kappa_\delta \end{bmatrix}, \tag{14}$$

$$\bar{x}_i^{(L)} \leq \bar{x}_i \leq \bar{x}_i^{(U)}, \quad i = 1, \ldots, N, \tag{15}$$

$$G_1(\bar{x}) = \begin{bmatrix} P_{out} \geq 10 \text{ kW} & \eta \geq 90\% & \text{pf} \geq 0.8 \end{bmatrix}, \tag{16}$$

$$G_2(\bar{x}) = \begin{bmatrix} P_{out} \geq 3 \text{ MW} & \eta \geq 97\% & \text{pf} \geq 0.8 \end{bmatrix}, \tag{17}$$

where $\bar{x}$ is the vector of design parameters, L and U are insignias to specify the lower and upper boundary limits, N is the total number of design parameters, and G_1 and G_2 are the inequality constraint vectors for 10 kW and 3 MW design requirements, respectively.

A total of 12 and 13 design parameters are varied for the 10-kW and 3-MW machines, respectively. Detailed information about the design parameters is provided in Table 4, while the optimisation procedure is set up as shown in Fig. 3. Based on some random starting population of the design variables, a conceptual model is constructed and analysed in the FEA programme and then passed on to an optimiser (VisualDOC suite [23]) to process in a loop until the convergence criteria for each problem are achieved. As earlier indicated, a

Table 4 Boundary conditions of design parameters

Design variables	$\bar{x}$	PM-FSM design			
		10 kW		3 MW	
		$x^{(L)}$	$x^{(U)}$	$x^{(L)}$	$x^{(U)}$
Current angle (deg.)	α	0	90	0	90
Current density (A/mm²)	J	1	5	1	5
Stator outer diameter (mm)	D_{out}	250	300	1550	1650
Stator inner diameter (mm)	D_{in}	162	180	1150	1250
Shaft diameter (mm)	D_{sh}	80	85	800	850
Stack length (mm)	l_{st}	90	180	600	1200
Airgap length (mm)	g	–	–	2.5	3
PM width (mm)	b_{pm}	5	10	35	70
Rotor pole width (mm)	b_{pr}	9	18	70	140
Slot opening width (mm)	b_{sls}	7.5	15	40	80
Stator yoke height (mm)	h_{ys}	7.5	15	37.5	75
Rotor yoke height (mm)	h_{yr}	7.5	15	40	80
Rotor tooth tapering factor	t_0	0.5	1	0.5	1

nonlinear 2-D magnetostatic FEA programme (SEMFEM) is engaged for the analyses. SEMFEM prides itself as fast and accurate for time-stepped static FEA simulation of electrical machines.

For the constrained MDO problems, a metaheuristic evolutionary algorithm—the nondominated sorting genetic
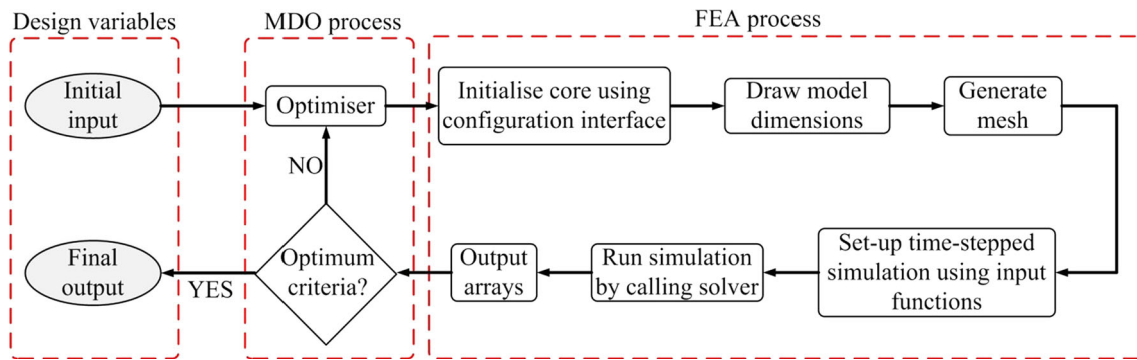
Fig. 3 An outline of the FEA-based design optimisation workflow used

algorithm II (NSGA-II)—proclaimed as "fast and elitist" is adopted [24]. NSGA-II has been applied to IMs [25], IPMs [26], brushless DFIGs [27] and WF-FSMs [28] for MDO problems, but not yet for PM-FSMs to the authors' best knowledge. The advantage of this algorithm is in its capacity to produce better spread of solutions to the truest convergence of the Pareto-optimal front for MDO problems, compared to other evolutionary algorithms. However, because they require greater function evaluations for convergence, they are very time-consuming when compared to deterministic methods. Besides, NSGA-II operates on the basis of certain genetic operators—mutation and crossover—that are applied to existing members of the population so as to evolve into new solutions. The populations keep evolving based on the prescribed boundaries, constraints and objective functions, until the allocated number of generations is exhausted and the simulation is terminated. In simple terms, NSGA-II functions by combining both standard parental populations and offspring populations formed first from the initial random population, and based on a prescribed selection operator capable of parameter fitness and spread, the next generations become more and more nondominated until the last iteration. The fast nondomination ranking is thus facilitated in terms of lower ranking order and/or lesser crowding behaviour of the offspring compared to the parent populations. Hence, for the professed MDO problems, the NSGA-II parameters are set forth as shown in Table 5. The difference observed in the mutation probability is due to difference in the number of design variables considered for each MDO problem category.

4 Execution and optimisation results

The constrained MDO problems are implemented for the 12/10 and 12/14 machines, at two different power levels—10 kW and 3 MW. For fair comparison, the same boundary conditions and parameter settings are applied to both the 12/10 and 12/14 machines, as already indicated in

Table 5 NSGA-II parameters

Parameters	PM-FSM design	
	10 kW	3 MW
Mutation probability	0.083	0.076
Crossover probability	0.9	0.9
Mutation distribution index	10	10
Crossover distribution index	20	20
Population size	25	25
Iterations	100	100

Tables 4 and 5, respectively. The average time taken for the simulation of the kW designs is 37.4 h on an i7-4770 CPU workstation, while that of the 3 MW designs cruise to around 65.4 h.

The optimisation results which evolved from the initial populations are evinced as shown in Figs. 4 and 5, respectively. It is clear from both figures that a level of compromise persists between the active mass and torque ripple. As expected, it is observed that the competing variables perform better for the 12/14 machine compared to the 12/10 machine at 10 kW power. However, any advantage acquired at 10 kW is traded off at 3 MW power. To articulate why this is the case, the researchers were drawn to carefully investigate the general behaviour of the optimal design candidates, especially at 3 MW power, by benchmarking five random optimal design candidates labelled "I–V" and representing the 12/10 machine and comparing their performance indices in per unit as shown in Fig. 6. The underlying factor in these benchmarks is based on designs that are able to match the power specification at 3 MW. The same selection process is repeated for the 12/14 machine leading to the benchmarks labelled "VI–X" as shown in Fig. 7. Lastly, another five optimal designs (XI–XV) shown in Fig. 8 are selected from the 12/14 optimal set. Note that, all the performance indices compared in Figs. 6, 7 and 8 are normalised with reference to

Fig. 4 Pareto-optimal design candidates for 10 kW PM-FSMs
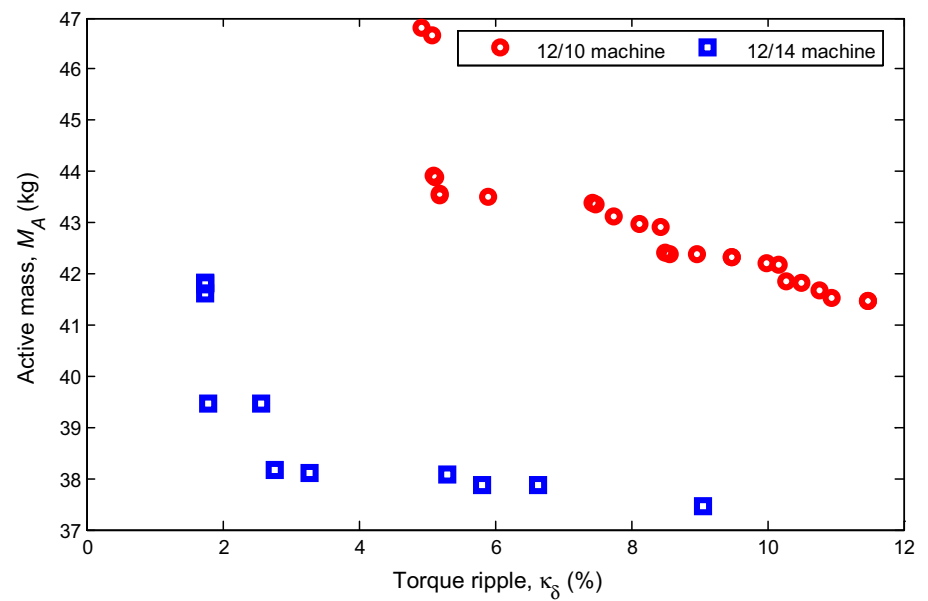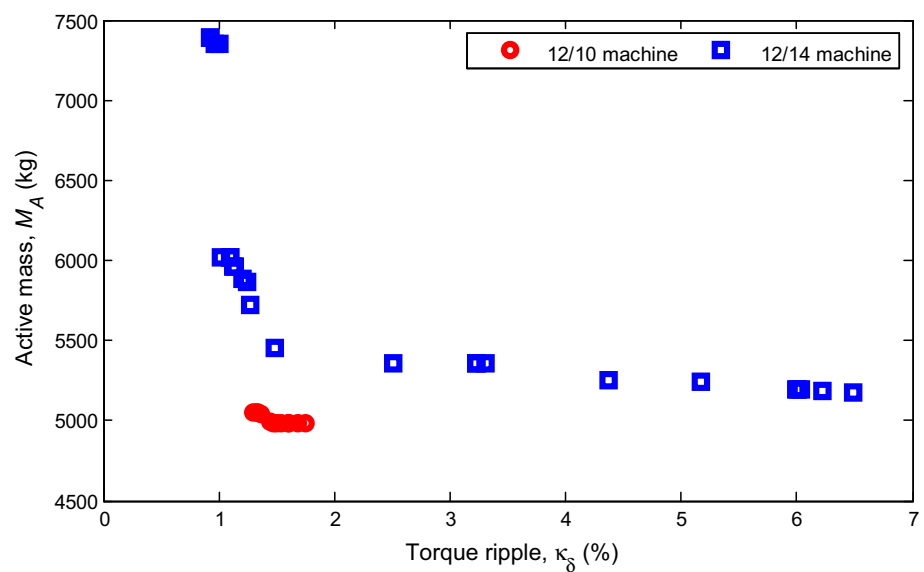

Fig. 5 Pareto-optimal design candidates for 3 MW PM-FSMs

the values of design I, e.g. the torque ripple value of design I is used as the reference in the design category—designs XI–XV.

Meanwhile, in the first category (designs I–V), Fig. 6 shows that most of the optimal selections exhibit almost similar performance characteristics because of the closely knitted optimal solution set depicted in Fig. 5. Whereas the second category (designs VI–X) in Fig. 7, which is dispersed by virtue of the optimal solutions, indicated along the Pareto-optimal front in Fig. 5, portray contrary characteristics of the torque ripples. Meanwhile, Fig. 7 also reveals that for the same reference power as the 12/10 machine, the optimum torque ripple values in the 12/14 machine become unusually high, reaching up to five times in one instance.

To provide further explanation on the behaviour of the 12/14 machines at 3 MW powers, which is observed to be at variance to what obtained in its 10-kW machines, Fig. 8 clearly shows that when the optimum torque ripple is sized to correspond to a counterpart 12/10 machine, the active mass is increased to about 20%. By comparing the optimal solutions of designs VI–X (obtained by baselining the output power to 3 MW) to those of designs XI–XV (obtained by baselining the torque ripple to that of design I), different charts of certain key design variables are generated as shown in Figs. 9, 10 and 11. Figures 9, 10 and 11 show that increase in PM volume, decrease in split ratio and decrease in current density are the main factors that constitute larger active mass in the 12/14 machines compared to the 12/10 ones at 3 MW power range.

Fig. 6 Performance comparison of optimum design candidates of 12/10 3-MW machines at normalised values and based on similar output power
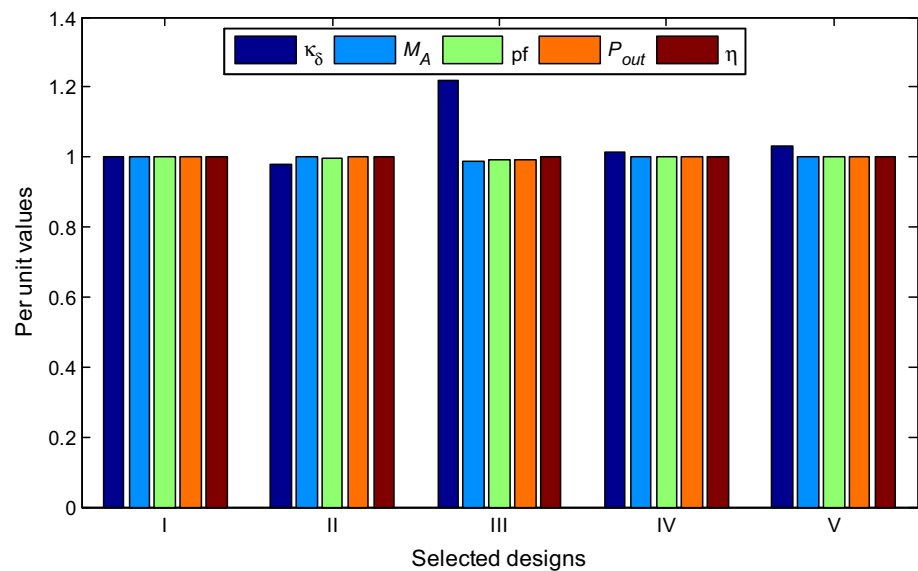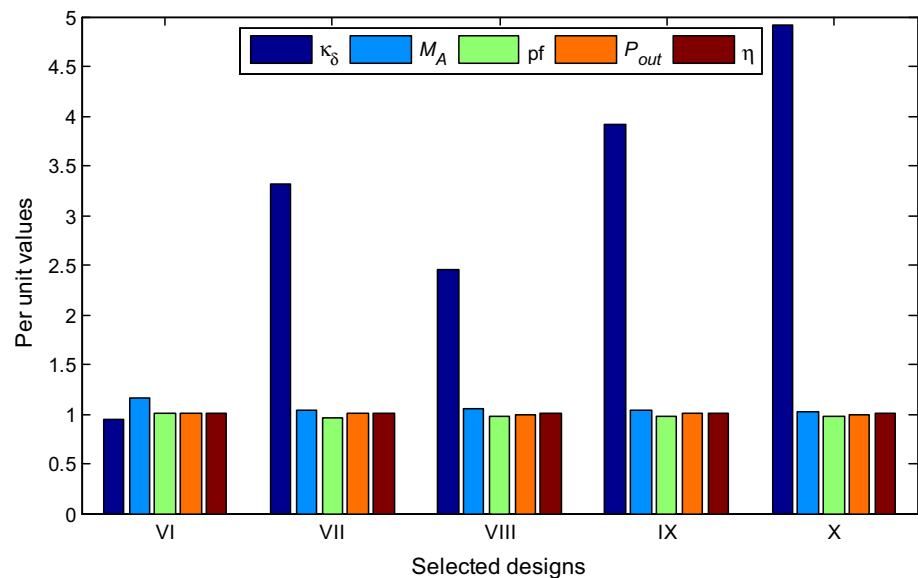

Fig. 7 Performance comparison of optimum design candidates of 12/14 3-MW machines at normalised values and based on the same output power

This is possible because, as indicated, the decrease in the current density of the 12/14 machines is observed to be very significant, up to two times less when compared to that in the 12/10 machines.

In addition, one can also observe a connection between the variations of the PM volume and the resulting torque ripple. For instance, torque ripple values in Figs. 6 and 8 are mostly low compared to those evaluated in Fig. 7, which when contrasted with the normalised PM volumes in Fig. 9, a pattern suggesting a corresponding effect on PM consumption is realised. Essentially, a higher PM usage increases the prominence of the torque ripple effects. However, the 3 MW 12/10 machines produce better trade-offs between the quantities of PM used and the generator active mass (Fig. 6 versus

Fig. 9), as well as yield an overall improvement in terms of the power density.

5 Benchmark comparison and 3-D FEA evaluation

In Table 6, four machines are benchmarked from the optimal design candidates presented in the preceding section—two selected from each machine at 3 MW optimal candidates and the other two selected *pari passu* from the 10-kW machines. The benchmarks are used to facilitate further comparison of the design characteristics of the understudied machines, based on approximation of certain design variables available

Fig. 8 Performance comparison of optimum design candidates of 12/14 3-MW machines at normalised values, based on the torque ripple of design I
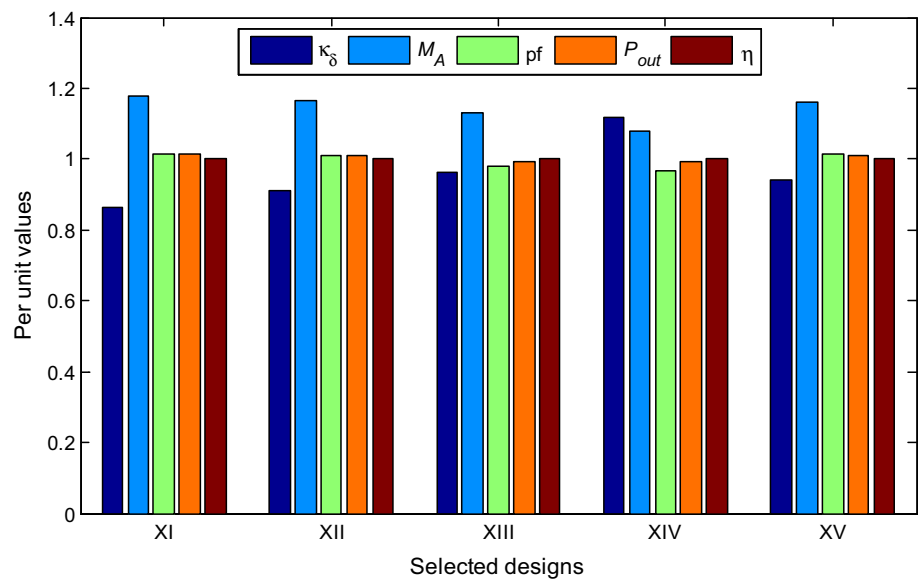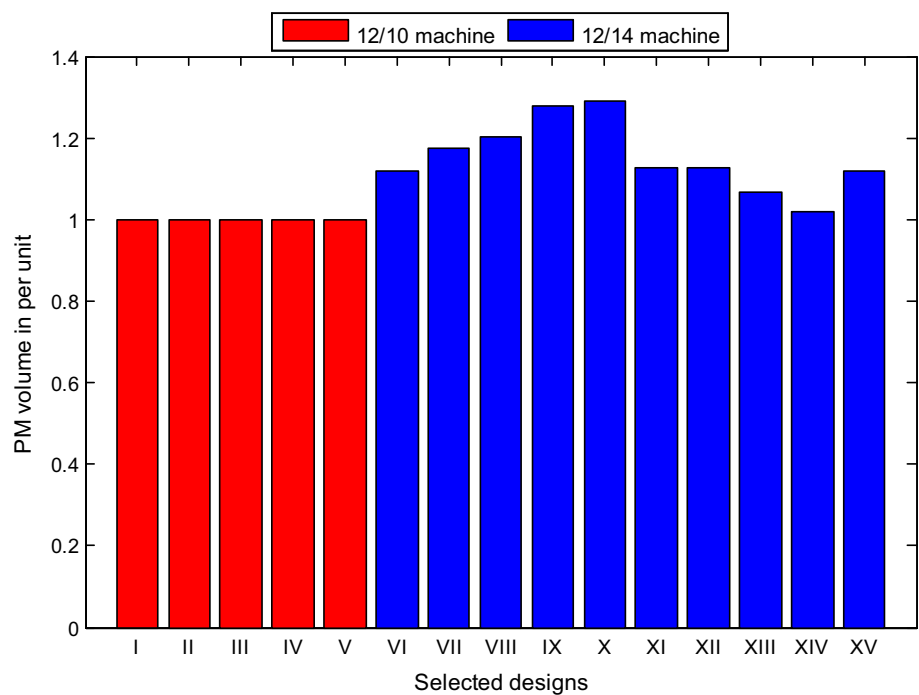

Fig. 9 Comparison of PM amount used in 3 MW optimum design candidates of 12/10 and 12/14 machines (1 per unit volume is the value of PM volume used in design I)

from data produced by the general MDO function evaluations. Thereafter, some of the selected benchmarks are further compared in terms of the time-stepped 2-D static FEA results to a 3-D transient FEA one.

5.1 Benchmark comparison

From Table 6, it is observed that at 3 MW output power, larger split (Λ_0) and aspect (κ_L) ratios evolve for the 12/10 machine, unlike its 12/14 counterpart. But at 10 kW, both the split and aspect ratios are fairly comparable for the highlighted machines. No doubt, this immediately gives some insight on the behaviour of the copper losses and current densities at the different power levels. Observe that the copper losses and current densities evolve to fairly the same values for the 10-kW machines but not for the 3-MW machines, due to a relatively smaller split ratio of the 12/14 machine at 3 MW. Perhaps, this may be due to the potential for higher core losses in the 12/14 machine which suppresses the current density, viz. the copper loss in order to satisfy the efficiency design limits, among other things.

Fig. 10 Split ratios in selected 3 MW optimum design candidates
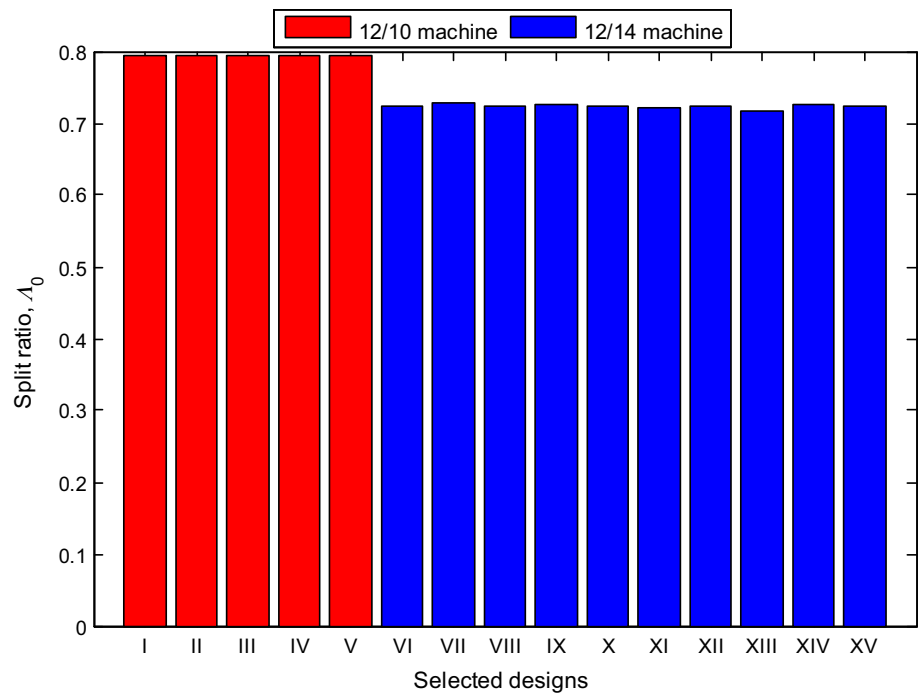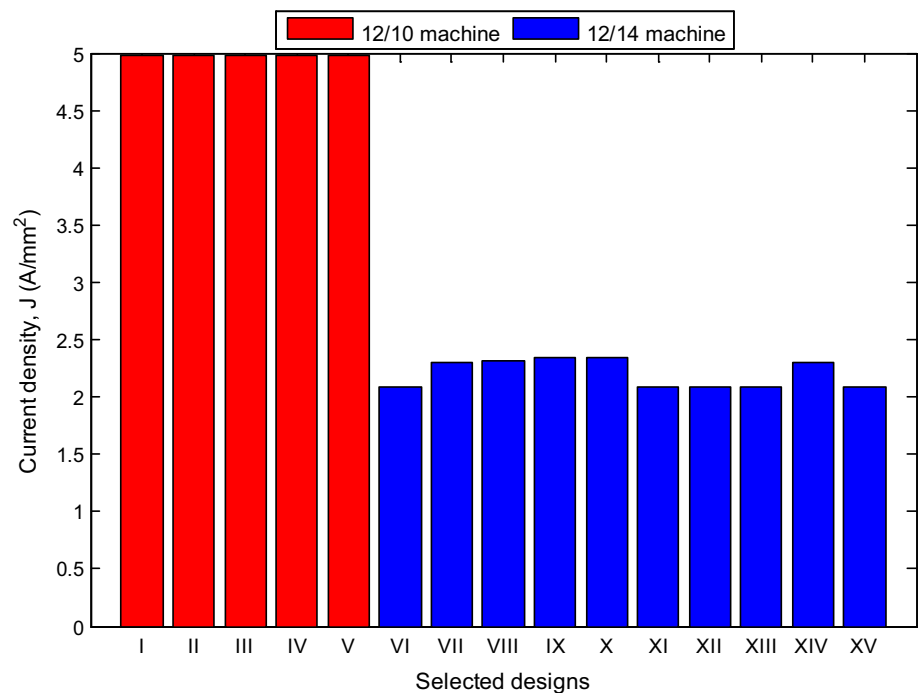

Fig. 11 Variation of current densities in selected 3 MW optimum design candidates

Also, one can observe that the torque densities for the 3-MW machines are more than two times, almost triple for the 12/10 machine compared to the 10-kW machines, thanks to the fixed rotor speed considered at both power levels. But while the torque density is higher for the 12/14 compared to the 12/10 at 10 kW, the outcome, as earlier indicated, is reversed at 3 MW, no thanks to trade-offs observed between the current densities and active masses. But considering the 10-kW machines and its fairly comparable design variables which evolved, it is safe to conclude that in order to stress the superior performance of the 12/14 machine compared to the 12/10 machine, especially in terms of torque density, both machines must be analysed with fairly similar design attributes.

Table 6 Nomination and comparison of optimum candidates used in 3-D FEA

Parameters	3-MW machines		10-kW machines	
	12/10: I	12/14: XIII	12/10	12/14
P_{out}	3	3	10.02	10.12
κ_δ (%)	1.31	1.27	5.73	5.88
M_A (kg)	5049.74	5719.16	43.57	37.86
η (%)	98.87	99.08	94.99	95.40
pf	0.82	0.80	0.83	0.81
Λ_0	0.79	0.56	0.56	0.60
κ_L	0.72	0.60	0.81	0.78
Nm/kg	15.52	13.40	5.99	6.93
J (A/mm^2)	4.97	2.08	4.99	4.99

On the other hand, the efficiency of the 12/10 machine is unexpectedly lower for both the 10-kW and 3-MW machines compared to their 12/14 counterparts. Such an outcome discredits the 1.4 times the fundamental frequency effect on the core losses which is supposedly detrimental to the 12/14 machine when compared to the 12/10 machine [19, 20]. It is believed that the observed discrepancy has more to do with the optimal condition of certain design variables, e.g. Λ_0, κ_L and J, when subjected to the MDO process, rather than in respect of the selection criterion which is based on similar torque ripple values. Besides, the researchers found with other optimal candidates that, even if the selection criteria were based on the other objective parameter, viz. similar active mass, the 12/10 machine is observed to generally operate at a slightly lower efficiency. However, to maintain higher efficiency, the 3 MW 12/14 machine experiences a decrease in power density due to a positive correlation approximated

for both the split ratio and current density with respect to the active mass in the MDO search space as later elucidated in Fig. 20.

Meanwhile, the efficiency and power factor are studied under varying load currents as shown in Fig. 12. At 45% load current, it is interesting to see that both machines can operate close to unity power factor and almost at peak efficiency in spite of the power levels. More importantly, the power factor specification (0.8) and efficiency specification (90% at 10 kW and 97% at 3 MW) can be generally surpassed for both machines in the observed load range. The only exception is the efficiency of the 3-MW machines which dominates in over just 80% of the load range, whereas the efficiency of the 12/10 machine is seen to improve when it is operating at less than 60% of the rated load current. In addition, the 3-MW machines show better and more stable efficiency at higher loads. Overall, there is an excellent off-peak performance of the optimally designed PM-FSMs to suit the proposed wind generator and its associated drivetrain components in terms of efficiency and power factor.

Table 7 Inductances and saliency ratios of optimum candidates

Parameters	3-MW machines		10-kW machines	
	12/10: I	12/14: XIII	12/10	12/14
α (deg.)	64.061	40.607	70.795	30.332
$I_{s(RMS)}$ (A)	103.714	75.020	11.673	11.466
L_d (mH)	564.017	590.309	114.894	93.759
L_q (mH)	284.477	609.676	64.356	114.241
s	0.504	1.032	0.560	1.218

Fig. 12 Plots showing PM-FSMs load current profiles against: **a** machine efficiency and **b** power factor (1 per unit current is in terms of rated current in respective machine)
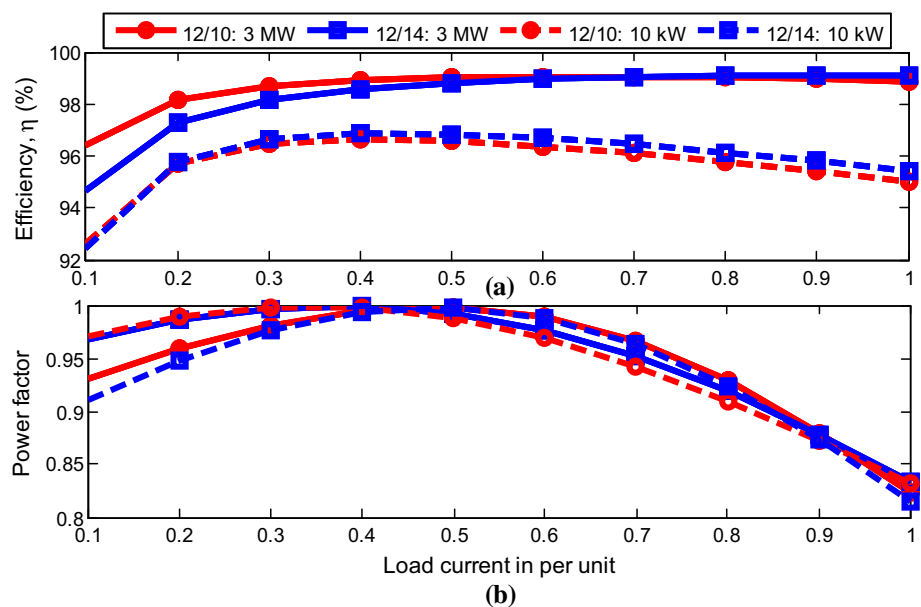
Fig. 13 Response of split ratio, slot opening width and rotor pole width to torque ripple approximated for 10 kW 12/10 PM-FSM solutions in the MDO space
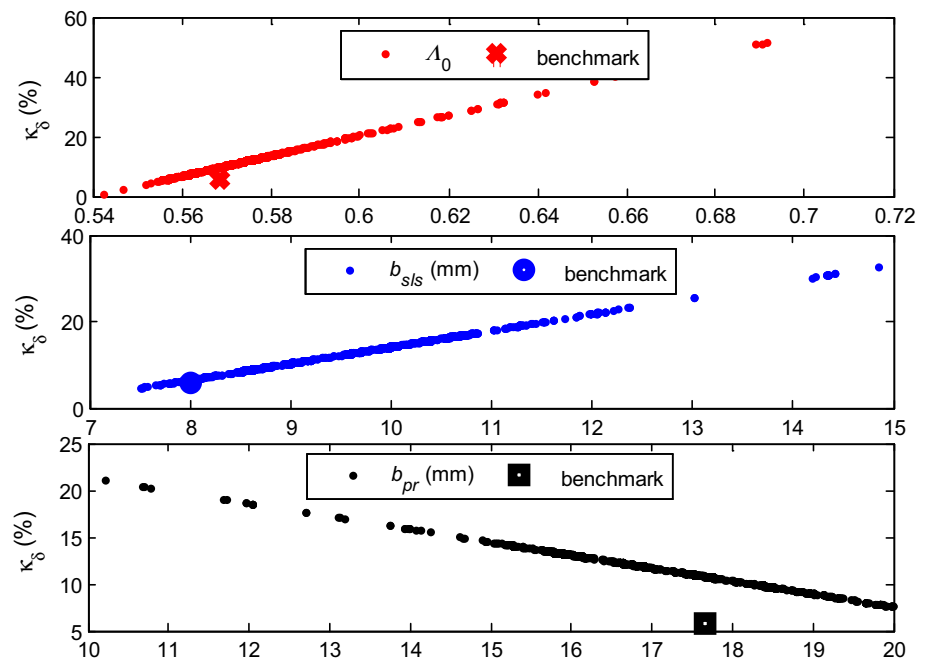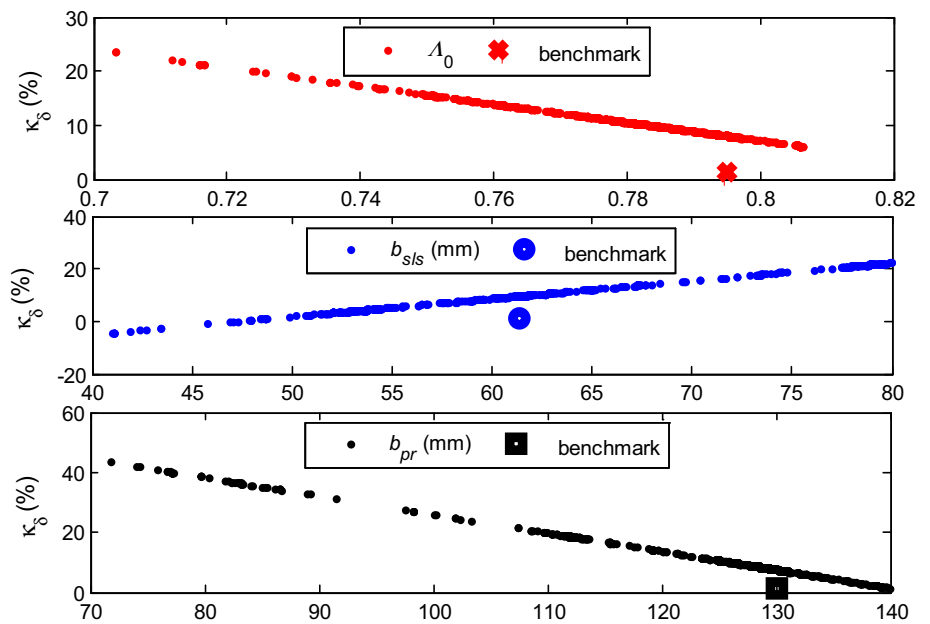

Fig. 14 Response of split ratio, slot opening width and rotor pole width to torque ripple approximated for 3 MW 12/10 PM-FSM solutions in the MDO space

Returning to Table 6, it is equally observed that the torque ripple values can be much lower in the 3-MW machines compared to the 10-kW machines, a situation which was earlier visualised in the Pareto-optimal plots in Figs. 4 and 5. It is therefore clearly indicated in Table 7 that this may be due to relatively lower saliency ratios (*s*) in the 3-MW machines compared to their 10-kW counterparts—10 and 15.2% for the 12/10 and 12/14 machines, respectively. This is another important finding especially since PM-FSMs, due to its double saliency structure, are notorious for high torque ripples.

It then means that, for utility-scale wind turbines, such concerns might be less worrisome for the considered PM-FSM wind generator designs.

In pursuit of the main objectives (minimum torque ripple and active mass) considered in this study, an investigation of the general behaviour of certain respective design variables was approximated in the feasible search region for the entire function evaluations in order to give additional insights on the performance trade-offs observed in the 10 kW and 3 MW designs. The results are reported as shown in Figs. 13, 14,

Fig. 15 Response of split ratio, slot opening width and rotor pole width to torque ripple approximated for 10 kW 12/14 PM-FSM solutions in the MDO space
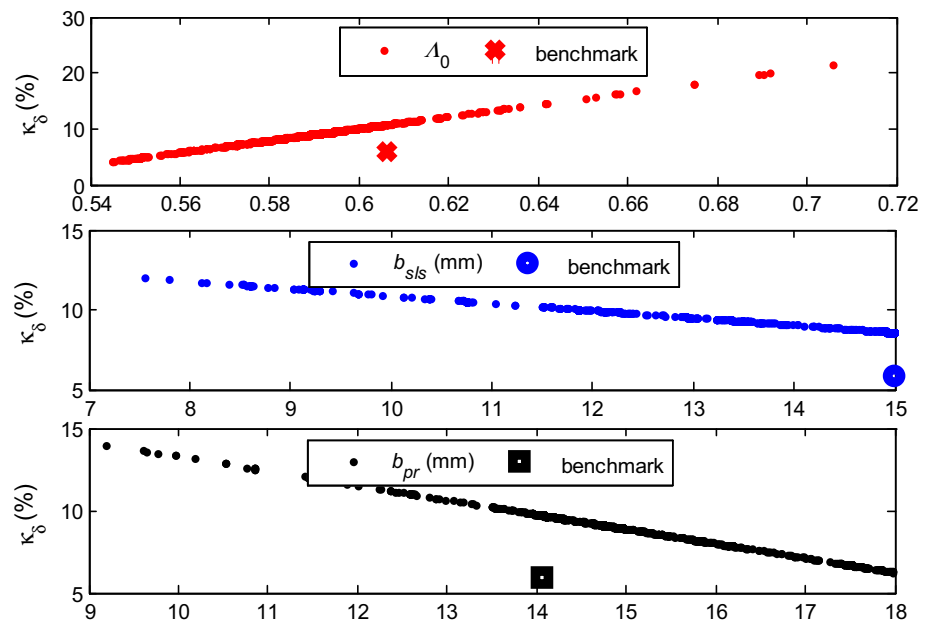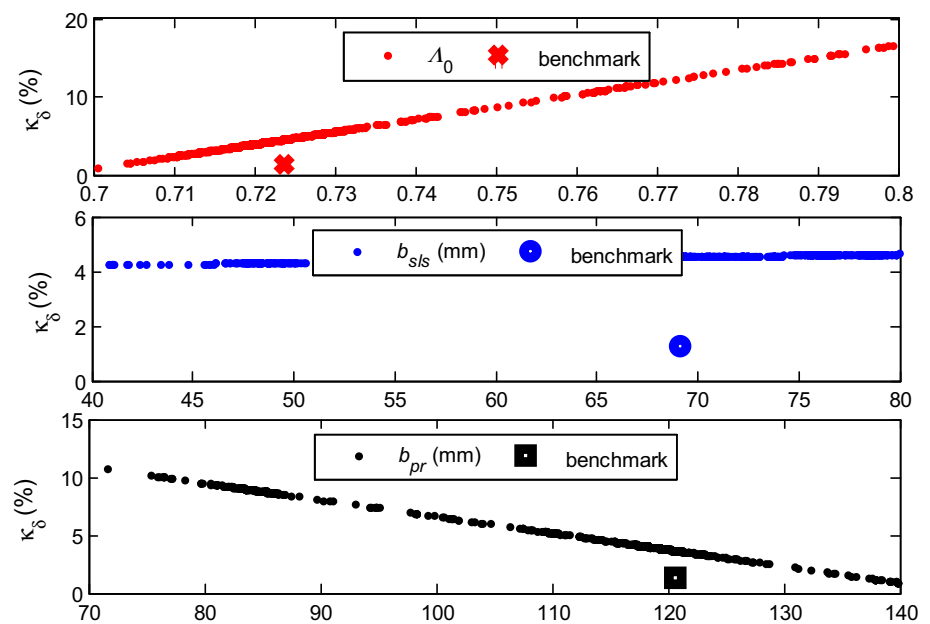

Fig. 16 Response of split ratio, slot opening width and rotor pole width to torque ripple approximated for 3 MW 12/14 PM-FSM solutions in the MDO space

15, 16, 17, 18, 19 and 20. For the 12/10 machines (Figs. 13, 14, 17, 18), the split ratio (Λ_0) is observed as a critical variable in the evaluated optimal torque ripple (κ_δ) and active mass (M_A) at the different power levels. As for the optimum performance of the 12/14 machines at 10 kW and 3 MW power levels, the slot opening width (b_{sls}) is the important variable for the evaluated torque ripple, while the split ratio, current density (J) and PM width (b_{pm}) are attributed to the estimated active mass. Within a specified power level, it is also clear to see that variation of the selected design variables is indicative of the differences observed between the objective performance of the 12/10 and 12/14 machines at these

power ranges. For instance, the slot opening width varies differently with respect to torque ripple for the 12/10 and 12/14 machines at 10 kW power, while at 3 MW power, it is the split ratio.

At this stage, it becomes difficult to streamline the superiority of the 12/10 machine over the 12/14 machine, or vice versa, because the performance of either machine appears to be more a function of the power level at which the design is undertaken. Granted, it is very clear that both machines possess more respectable performance characteristics at 3 MW power than at 10 kW. Suffice to say that the superior performance of the 3-MW machines, compared to the 10-kW

Fig. 17 Response of split ratio, current density and PM width to active mass approximated for 10 kW 12/10 PM-FSM solutions in the MDO space
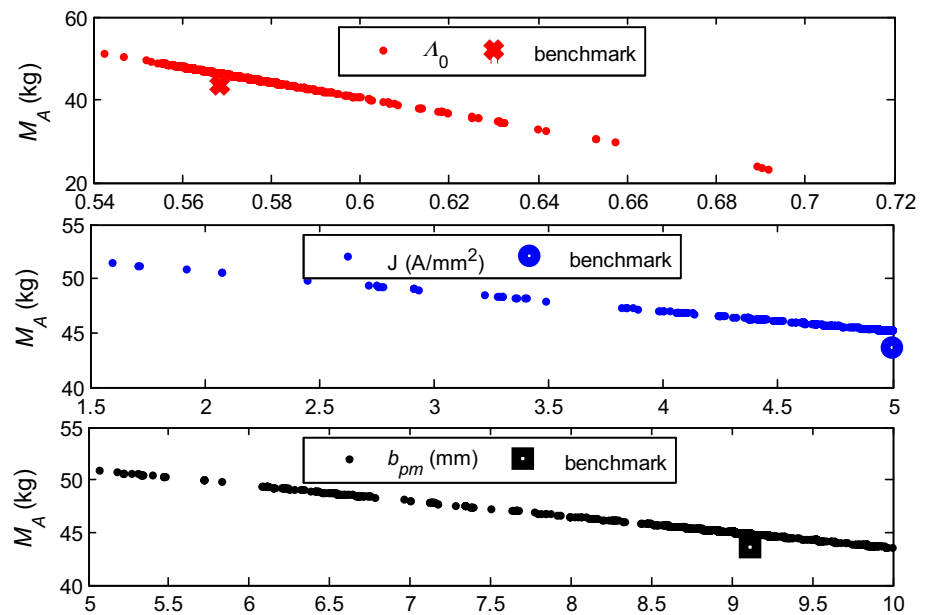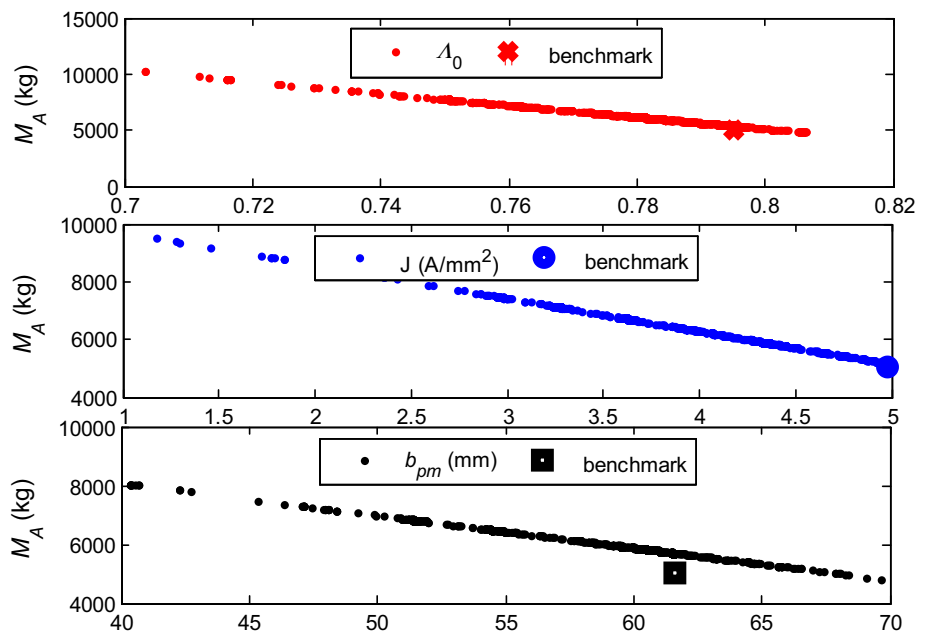

Fig. 18 Response of split ratio, current density and PM width to active mass approximated for 3 MW 12/10 PM-FSM solutions in the MDO space

machines, is an indication of inherent declaration of the candidature of the studied PM-FSMs for the proposed geared MS wind power generators.

5.2 2-D FEA versus 3-D FEA evaluation

To limit the computation time for the 3-D FEA modelling, quarter symmetry is employed. Hence, the flux density maps of the constructed 3-D models are as shown in Fig. 21. In addition, a comparison of 2-D and 3-D FEA result of the average electromagnetic torque considered from no-load to rated is made for both machines as shown in Fig. 22. A good

agreement is witnessed generally, but with slight deviation observed towards the rated load, in both machines. No doubt, this discrepancy at higher load profiles is due to worsening end leakages, which are not fully accounted for in the 2-D FEA modelling. Observe that an increase in the load current increases the saturation effects in the 3-D cores, viz. the end-leakage flux due mostly to fringing along the axial direction, which was not practically conceived in the 2-D models. Essentially, an estimation of the discrepancy is given in the range of 4–8% of the compared 3-MW machines, which, if taken into account, could assist in accurately modelling for such effects in 2-D FEA.

Fig. 19 Response of split ratio, current density and PM width to active mass approximated for 10 kW 12/14 PM-FSM solutions in the MDO space
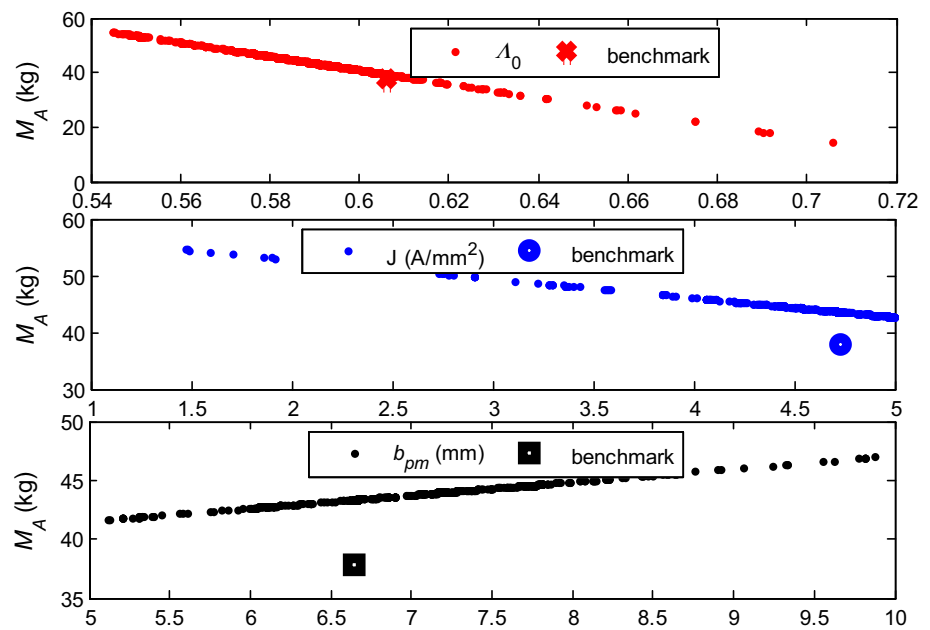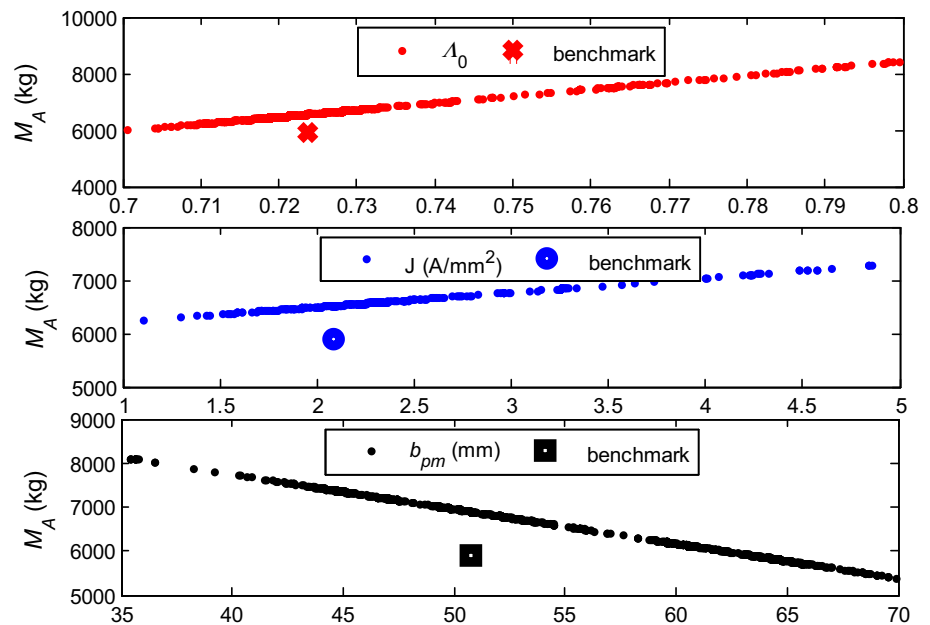

Fig. 20 Response of split ratio, current density and PM width to active mass approximated for 3 MW 12/14 PM-FSM solutions in the MDO space

6 Conclusion

In this paper, the design evaluation of optimum rare-earth PM-FSMs at 10 kW and 3 MW has been investigated for geared medium-speed wind generator drives. The design approach, machine topologies and MDO strategy have been clearly presented. Based on FEA, two PM-FSM topologies—12/10 and 12/14—were optimised and compared at the prescribed power levels. The result shows that the torque ripple values in the 3-MW machines can be much lower compared to the 10-kW machines due to observed differences in their saliency ratios and with significantly higher torque

densities recorded in the latter thanks to the constant medium-speed drivetrain maintained at both power levels. To this end, an indication of the high potentials of the proposed PM-FSMs for geared MS wind generator drives in large-scale wind turbine systems has been established, which makes them eligible for even rare-earth-free excitation sources like ferrite PMs or wound fields.

Moreover, it is observed that the superior optimum performance of the 12/14 machine compared to the 12/10 machine at 10 kW power is interchanged at 3 MW powers, due to a significant decrease in the current densities of the former which result in increase in both the torque ripple and active
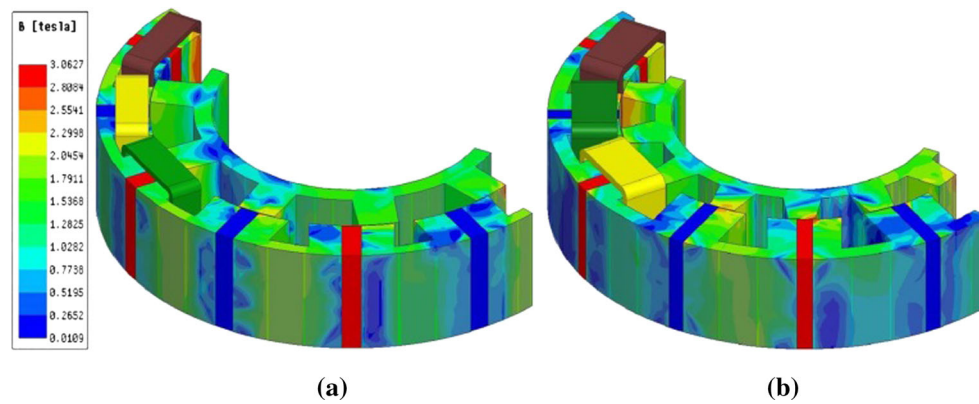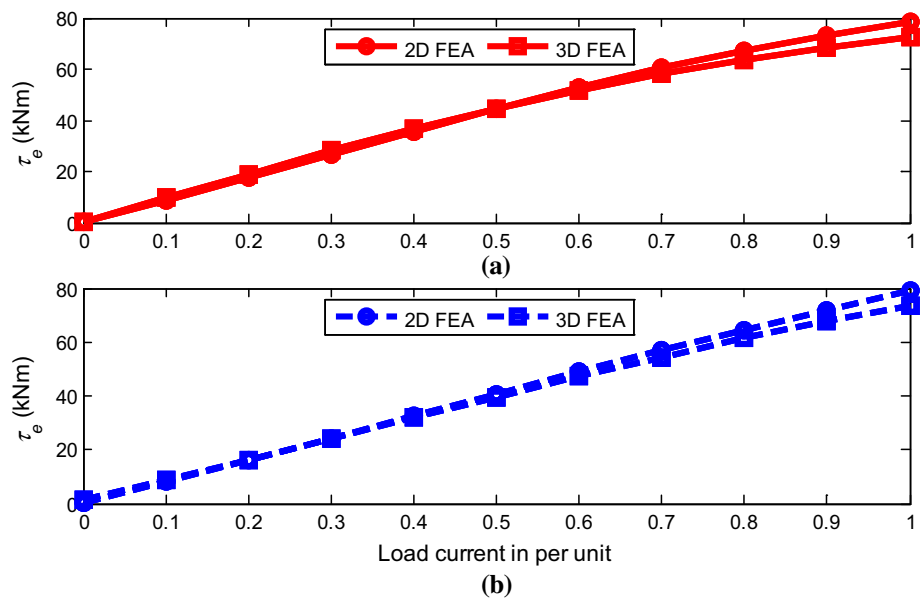
Fig. 21 Flux density map of 3 MW PM-FSMs at rated conditions, analysed in 3-D transient FEA showing plots of: **a** the 12/10 machine frozen at 5.21 ms and **b** the 12/14 machine frozen at 5.44 ms

Fig. 22 Load current versus torque characteristics of 3 MW PM-FSMs displayed for: **a** 12/10 machine and **b** 12/14 machine (1 per unit current is in terms of rated current in respective machine)

mass. A connection is also observed between the variations of PM volume and the resulting torque ripple at 3 MW such that the higher the PM usage, the more prominent the torque ripple effects. Equally, it is clearly shown that the variation of selected design variables such as the split ratio, slot opening width, current density and PM width is reflective of the differences observed between the objective performance of the 12/10 and 12/14 machines at the studied power ranges.

Based on the MDO environment, it is equally established that the fundamental frequency of the 12/14 machine, which theoretically surpasses that of the 12/10 machine by a factor of 1.4 and with corresponding effect on the core loss, is not particularly detrimental to its efficiency. This trend was generally observed in all the optimal solutions and at the considered power levels. However, it must be said that the power densities of the 3 MW 12/14 machines are reduced compared to its 12/10 counterparts. This is due to an observed positive correlation plotted for both the split ratio and cur-

rent density against the active mass when the general function evaluations entertained in the MDO search space are approximated. Eventually, some selections from the 3 MW optimal candidates are compared between their 2-D static and 3-D transient FEA results, with good confidence displayed.

References

1. Schmidt S, Vath A (2012) Comparison of existing medium-speed drive train concepts with a differential gearbox approach. European Wind Energy Association, Copenhagen
2. Zhang J, Cheng M, Chen Z, Hua W (2009) Comparison of stator-mounted permanent-magnet machines based on a general power equation. IEEE Trans Energy Convers 24(4):826–834
3. Zhu ZQ, Wu ZZ, Evans DJ, Chu WQ (2015) A wound field switched flux machine with field and armature windings separately wound in double stators. IEEE Trans Energy Convers 30(2):772–783
4. Hua W, Cheng M, Zhu ZQ, Zhao W, Kong X (2008) Comparison of electromagnetic performance of brushless motors having magnets in stator and rotor. J Appl Phys 103(7):07F124-3

5. Zulu A, Mecrow BC, Armstrong M (2010) A wound-field three-phase flux-switching synchronous motor with all excitation sources on the stator. IEEE Trans Ind Appl 46(6):2363–2371

6. Shao L, Hua W, Zhu ZQ, Zhu X, Cheng M, Wu Z (2017) A novel flux-switching permanent magnet machine with overlapping windings. IEEE Trans Energy Convers 32(1):172–183

7. Wu ZZ, Zhu ZQ (2015) Analysis of air-gap field modulation and magnetic gearing effects in switched flux permanent magnet machines. IEEE Trans Magn 51(5):1–12

8. Somesan LE, Viorel IA (2013) Permanent magnet flux-switching machine, optimal design and performance analysis. Adv Electr Eng 11(2):46–53

9. Cao R, Mi C, Cheng M (2012) Quantitative comparison of flux-switching permanent-magnet motors with interior permanent magnet motor for EV, HEV, and PHEV applications. IEEE Trans Magn 48(8):2374–2384

10. Zhu ZQ, Al-Ani MMJ, Liu X, Lee B (2015) A mechanical flux weakening method for switched flux permanent magnet machines. IEEE Trans Energy Convers 30(2):806–815

11. Dobzhanskyi O, Gottipati P, Karaman E, Xiaozhong L, Mendrela EA, Trzynadlowski AM (2012) Multilayer-winding versus switched-flux permanent-magnet ac machines for gearless applications in clean-energy systems. IEEE Trans Ind Appl 48(6):2296–2302

12. Yan J, Lin H, Huang Y, Liu H, Zhu ZQ (2009) Magnetic field analysis of a novel flux switching transverse flux permanent magnet wind generator with 3-D FEM. In: PEDS Taiwan, pp 332–335

13. Hao L, Lin M, Zhao X, Fu X, Zhu ZQ, Jin P (2012) Static characteristics analysis and experimental study of a novel axial field flux-switching permanent magnet generator. IEEE Trans Magn 48(11):4212–4215

14. Lin M, Hao L, Li X, Zhao X, Zhu ZQ (2011) A novel axial field flux switching permanent magnet wind power generator. IEEE Trans Magn 47(10):4457–4460

15. Wang Y, Sun J, Zou Z, Wang Z, Chau KT (2013) Design and analysis of a HTS flux-switching machine for wind energy conversion. IEEE Trans Appl Supercond 23(3):5000904

16. Yu C, Niu S (2015) Development of a magnetless flux switching machine for rooftop wind power generation. IEEE Trans Energy Convers 30(4):1703–1711

17. Thomas AS, Zhu ZQ, Jewell GW (2011) Comparison of flux switching and surface mounted permanent magnet generators for high-speed applications. IET Electr Syst Transp 1(3):111–116

18. Akuru UB, Kamper MJ (2015) Comparative advantage of flux switching PM machines for medium-speed wind drives. In: DUE Cape Town, pp 149–154

19. Akuru UB, Kamper MJ (2015) Evaluation of flux switching PM machines for medium-speed wind generator drives. In: IEEE ECCE Canada, pp 1925–1931

20. Anyuan C, Rotevatn N, Nilssen R, Nysveen A (2009) Characteristic investigations of a new three-phase flux-switching permanent magnet machine by FEM simulations and experimental verification. In: ICEMS Japan, pp 1–6

21. Wei H, Ming C, Zhu ZQ, Howe D (2006) Design of flux-switching permanent magnet machine considering the limitation of inverter and flux-weakening capability. In: Industry application conference and 41st IAS annual meeting conference record Florida, vol 5, pp 2403–2410

22. SEMFEM documentation. http://www0.sun.ac.za/semfem/index.html. Accessed 27 June 2018

23. VisualDOC User's Manual (2017) Version 8.0. Vanderplaats Research & Development Inc, Colorado Springs, CO, USA

24. Deb K, Pratap A, Agarwal S, Meyarivan T (2002) A fast and elitist multiobjective genetic algorithm: NSGA-II. IEEE Trans Evol Comput 6(2):182–197

25. Le Besnerais J, Lanfranchi V, Hecquet M, Brochet P (2008) Multiobjective optimization of induction machines including mixed variables and noise minimization. IEEE Trans Magn 44(6):1102–1105

26. Jannot X, Vannier J, Marchand C, Gabsi M, Saint-Michel J, Sadarnac D (2011) Multiphysic modeling of a high-speed interior permanent magnet synchronous machine for a multiobjective optimal design. IEEE Trans Energy Convers 26(2):457–467

27. Wang X, Strous TD, Lahaye D, Polinder H, Ferreira JA (2016) Modeling and optimization of brushless doubly-fed induction machines using computationally efficient finite-element analysis. IEEE Trans Ind Appl 52(6):4525–4534

28. Akuru UB, Kamper MJ (2017) Formulation and multi-objective design optimisation of wound-field flux switching machines for wind energy drives. IEEE Trans Ind Electron 65(2):1828–1836